Bistable Multifunctionality and Switchable Strong Ferromagnetic-to-Antiferromagnetic Coupling in a One-Dimensional Rhodium(I)−Semiquinonato Complex

Minoru Mitsumi,*,[†,‡] Takashi Nishitani,[†] Shota Yamasaki,[†] Nayuta Shimada,[†] Yuuki Komatsu,[†] Koshiro Toriumi,[†,‡] Yasutaka Kitagawa,*,[⊥] Mitsutaka Okumura,[⊥] Yuji Miyazaki,*,[∥] Natalia Górska,[∥,¶] Akira Inaba,[∥] Akinori Kanda,[§] and Noriaki Hanasaki[§]

[†]Department of Material Science and [‡]Research Center for New Functional Materials, Graduate School of Material Science, University of Hyogo, 3-2-1 Kouto, Kamigori-cho, Ako-gun, Hyogo 678-1297, Japan
[⊥]Department of Chemistry, [∥]Research Center for Structural Thermodynamics, and [§]Department of Physics, Graduate School of Science, Osaka University, Machikaneyama, Toyonaka, Osaka 560-0043, Japan

Ⓢ Supporting Information

ABSTRACT: We present a comprehensive study of the synthesis, heat capacity, crystal structures, UV−vis−NIR and mid-IR spectra, DFT calculations, and magnetic and electrical properties of a one-dimensional (1D) rhodium(I)−semiquinonato complex, $[Rh(3,6\text{-DBSQ-}4,5\text{-}(MeO)_2)(CO)_2]_\infty$ (**3**), where 3,6-DBSQ-4,5-$(MeO)_2{}^{\bullet-}$ represents 3,6-di-*tert*-butyl-4,5-dimethoxy-1,2-benzosemiquinonato radical anion. The compound **3** comprises neutral 1D chains of complex molecules stacked in a staggered arrangement with short Rh−Rh distances of 3.0796(4) and 3.1045(4) Å at 226 K and exhibits unprecedented bistable multifunctionality with respect to its magnetic and conductive properties in the temperature range of 228−207 K. The observed bistability results from the thermal hysteresis across a first-order phase transition, and the transition accompanies the exchange of the interchain C−H···O hydrogen-bond partners between the semiquinonato ligands. The strong overlaps of the complex molecules lead to unusually strong ferromagnetic interactions in the low-temperature (LT) phase. Furthermore, the magnetic interactions in the 1D chain drastically change from strongly ferromagnetic in the LT phase to antiferromagnetic in the room-temperature (RT) phase with hysteresis. In addition, the compound **3** exhibits long-range antiferromagnetic ordering between the ferromagnetic chains and spontaneous magnetization because of spin canting (canted antiferromagnetism) at a transition temperature T_N of 14.2 K. The electrical conductivity of **3** at 300 K is 4.8×10^{-4} S cm^{-1}, which is relatively high despite Rh not being in a mixed-valence state. The temperature dependence of electrical resistivity also exhibits a clear hysteresis across the first-order phase transition. Furthermore, the ferromagnetic LT phase can be easily stabilized up to RT by the application of a relatively weak applied pressure of 1.4 kbar, which reflects the bistable characteristics and demonstrates the simultaneous control of multifunctionality through external perturbation.
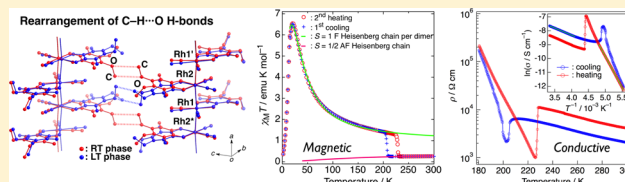
INTRODUCTION

The development of molecular materials that exhibit multifunctionality such as magnetic, electrical, dielectric, or optical properties has received increased attention from both fundamental and applied points of view.[1−5] A mutual interplay or synergy between these physical properties is important to further improve the functionality of these materials. Thus, the utilization of a single-component molecule is considered to be more advantageous than the utilization of a multicomponent system.[6−9] However, a minute molecular design about how to induce such a mutual interplay or synergy between the physical properties in the single-component molecule is required. Furthermore, in addition to the mutual interplay or synergy, control of physical properties through external perturbation is very effective for the simultaneous control of multifunctionality. Bistability is a fundamental phenomenon observed in materials in which two different states i.e., the ground and metastable

states, can coexist within a certain range of an external perturbation, such as a change in the temperature, pressure, and light irradiation, resulting from cooperative intermolecular interactions.[10−18] Interconversion between two energetically close-lying electronic states in a bistable system has fascinated material scientists for the development of future information storage and switching devices because the relative populations of the two states with different physical properties, such as magnetic, electrical, dielectric, or optical properties, can be controlled through changes in external perturbation.[19−27] Recently, novel bistable multifunctional electronic and magnetic materials have attracted considerable interest owing to their potential use in new types of electronic devices, where their multiple physical properties can be used for writing,

reading, and transferring information. Haddon and co-workers reported that ethyl- and *n*-butyl-substituted spirobiphenalenyl radicals simultaneously exhibit bistability in their magnetic, electrical, and optical properties, which has rarely been realized in a single-component molecular system.[28,29] This discovery has led to rapid advancements in the exploration of bistable multifunctional materials.[30−34]

To develop novel types of multifunctional single-component molecular materials that simultaneously exhibit both magnetic and electrical properties, we focused on a one-dimensional (1D) rhodium(I)−semiquinonato complex with a linear rhodium chain, $[Rh(3,6\text{-}DBSQ)(CO)_2]_\infty$ (**1**; 3,6-DBSQ$^{\bullet-}$ = 3,6-di-*tert*-butyl-1,2-benzosemiquinonato), as a basic component.[35,36] Semiquinonate is an organic radical anion and is one of the redox series of dioxolene, which can produce three different redox isomers, i.e., benzoquinone (BQ), semi-quinonate (SQ$^{\bullet-}$), and catecholate (Cat^{2-}), via two sequential one-electron transfers. Furthermore, several metal−dioxolene complexes that possess very close energy levels between the frontier orbitals of the metal d and dioxolene π^* orbitals are known to exhibit intramolecular charge transfer between the metal and ligand, which is known as valence tautomerism.[37] Such a valence tautomerism can be used to vary multiple physical properties.[38,39] In our target system, the semi-quinonato radical can serve not only as a carrier of $S = 1/2$ spin but also as an electron acceptor for the partial oxidation of a rhodium(I) linear chain. Thus, the linear rhodium chain can produce the 1D conducting d band via the charge transfer from the rhodium(I) ion to the semiquinonato ligand, i.e., the partial oxidation of the rhodium linear chain. In addition, the filling of the 1D d band can be controlled in cases where the application of an external perturbation, such as heat, pressure, or light irradiation, can control valence tautomerism. Using this strategy, we achieved control of the frontier orbital energy that adjusts the energy level of the vacant semiquinonato ligand π^* orbital to that of the filled 1D d band by introducing two electron-withdrawing chloro substituents at the 4 and 5 positions of the 3,6-DBSQ$^{\bullet-}$ ligand.[40] Consequently, a 1D mixed-valence rhodium(I,II)−semiquinonato/catecholato complex $[Rh(3,6\text{-}DBDiox\text{-}4,5\text{-}Cl_2)(CO)_2]_\infty$ (**2**), where 3,6-DBDiox-4,5-Cl$_2$ indicates 3,6-di-*tert*-butyl-4,5-dichloro-1,2-ben-zosemiquinonato or 3,6-di-*tert*-butyl-4,5-dichlorocatecholato, has been realized by the charge transfer from the rhodium(I) ion to the vacant semiquinonato ligand. The average formal oxidation state of the rhodium ion is +1.33, and the compound is a paramagnetic semiconductor with a significantly higher electrical conductivity of σ_{RT} = 17−34 S cm^{-1} at room temperature (RT). On the other hand, we found that the replacement of two chloro substituents with two methoxy groups at the 4 and 5 positions of the 3,6-DBSQ$^{\bullet-}$ ligand led to a drastic change in the magnetic and electrical properties of the 1D rhodium(I)−semiquinonato complex, $[Rh(3,6\text{-}DBSQ\text{-}4,5\text{-}(MeO)_2)(CO)_2]_\infty$ (**3**; 3,6-DBSQ-4,5-(MeO)$_2{}^{\bullet-}$ = 3,6-di-*tert*-butyl-4,5-dimethoxy-1,2-benzosemiquinonato),[41] although the basic skeletons of the Rh(3,6-DBSQ)(CO)$_2$ moieties are almost the same among the compounds **1**−**3**.[35,40]

Herein, we report a comprehensive study of the synthesis, heat capacity, X-ray photoelectron spectroscopy (XPS), crystal structures, UV−vis−NIR and mid-IR spectroscopy, and magnetic and electrical properties of the compound **3**. We also demonstrate unprecedented bistable multifunctionality of **3** based on its magnetic and conductive properties observed in the temperature range of 228−207 K. The single-crystal X-ray

crystal structure analyses revealed that the bistability results from the thermal hysteresis across a first-order phase transition; moreover, the transition accompanies an unexpected exchange of interchain C−H···O hydrogen-bond partners between semiquinonato ligands. The strong overlap of complex molecules in the 1D chain lead to unusually strong ferromagnetic interactions in the low-temperature (LT) phase; moreover, the compound **3** exhibits switching of its magnetic interactions from strong ferromagnetic in the LT phase to antiferromagnetic in the RT phase, with hysteresis. In addition, **3** undergoes long-range antiferromagnetic ordering between the ferromagnetic chains and spontaneous magnet-ization because of spin canting (canted antiferromagnetism) at a transition temperature T_N of 14.2 K. Furthermore, **3** exhibits relatively high electrical conductivity at RT despite Rh not being in a mixed-valence state. The temperature dependence of electrical resistivity also demonstrates a clear hysteresis, i.e., bistability, across the first-order phase transition, in addition to the magnetic bistability. We also performed density functional theory (DFT) calculations based on cluster models to examine the electronic structure and magnetic interactions in the compound **3**.

RESULTS AND DISCUSSION

Heat Capacity. The heat capacity of the compound **3** was measured by adiabatic calorimetry (Figure 1).[42] An intense heat
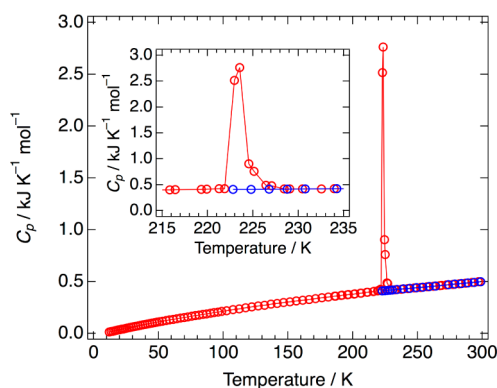

Figure 1. Molar heat capacity of $[Rh(3,6\text{-}DBSQ\text{-}4,5\text{-}(MeO)_2)\text{-}(CO)_2]_\infty$ (**3**) as a function of temperature. Red circles represent the data obtained after the sample was cooled to 12 K. Blue circles represent the data obtained after the sample was cooled to 222.8 K and show the supercooling of the RT phase. The inset shows an enlarged view of the heat capacity peak.

capacity peak due to the first-order phase transition was observed at 223.5 K during heating, indicating the presence of RT and LT phases. The first-order nature of this transition was also confirmed by the differential scanning calorimetry (DSC), in which endothermic and exothermic peaks were observed at 224 and 198 K, respectively (Figure S1). The enthalpy and entropy of the phase transition were determined to be 3.939(8) kJ mol^{-1} and 17.62(5) J K^{-1} mol^{-1}, respectively. If the observed entropy is assumed to arise from the $S = 1/2$ spins of the semiquinonato ligands alone, the actual entropy acquisition is substantially greater than the entropy gain $\Delta S = R \ln 2$ = 5.76 J K^{-1} mol^{-1}, which is expected for an $S = 1/2$ spin state. Although the present compound **3** exhibits a drastic structural change that accompanies the phase transition, as will be described in the X-ray Crystal Structure Analyses section,

distinct structural disorder that would contribute to the entropy gain was not apparently observed. For spin-crossover complexes, the phase transition is usually not accompanied by a change in the space group; moreover, its entropy is known to arise from changes in intramolecular and lattice vibrations perturbed by intermolecular interactions, in addition to the entropy gain due to the change in spin multiplicity.[43] Thus, as a possible origin of the observed entropy, similar changes in the intramolecular and lattice vibrations may contribute to the excess entropy observed in **3**, in addition to certain contribution from the $S = 1/2$ spins.

X-ray Photoelectron Spectroscopy. To examine the valence state of the rhodium atoms, we measured the XPS spectrum of **3** at RT as well as those of the rhodium(I)−semiquinonato complex, $[Rh^I(3,6\text{-}DBSQ)(CO)_2]_\infty$ (**1**), and the mixed-valence rhodium(I,II)−semiquinonato/catecholato complex, $[Rh^{I,II}(3,6\text{-}DBDiox\text{-}4,5\text{-}Cl_2)(CO)_2]_\infty$ (**2**).[40] The Rh $3d_{5/2}$ and $3d_{3/2}$ core-level spectra for these compounds are shown in Figure 2, and their binding energies are summarized
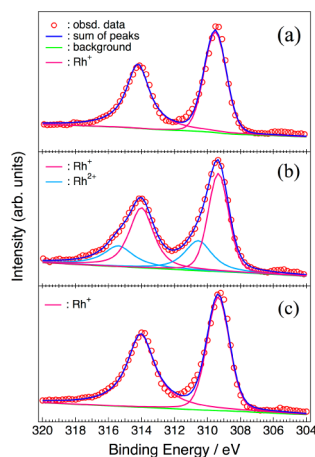
Figure 2. Rh $3d_{5/2}$ and $3d_{3/2}$ core-level spectra for (a) $[Rh^I(3,6\text{-}DBSQ)(CO)_2]_\infty$ (**1**), (b) $[Rh^{I,II}(3,6\text{-}DBDiox\text{-}4,5\text{-}Cl_2)(CO)_2]_\infty$ (**2**),[40] and (c) $[Rh(3,6\text{-}DBSQ\text{-}4,5\text{-}(MeO)_2)(CO)_2]_\infty$ (**3**). The solid lines are the deconvoluted components and the sum of all the components.

in Table 1. The rhodium(I)−semiquinonato complex **1** shows sharp Rh $3d_{5/2}$ and $3d_{3/2}$ peaks, whereas peaks of the mixed-valence rhodium(I,II)−semiquinonato/catecholato complex **2** are broad compared to **1** and could be resolved into two sets of Rh$^+$ $3d_{5/2,3/2}$ and Rh^{2+} $3d_{5/2,3/2}$ doublets through curve

Table 1. XPS Data for $[Rh^I(3,6\text{-}DBSQ)(CO)_2]_\infty$ (1), $[Rh^{I,II}(3,6\text{-}DBDiox\text{-}4,5\text{-}Cl_2)(CO)_2]_\infty$ (2),[40] and $[Rh(3,6\text{-}DBSQ\text{-}4,5\text{-}(MeO)_2)(CO)_2]_\infty$ (3)

|	binding energies, eV[a,b]			
compd	Rh$^+$ $3d_{5/2}$	Rh^{2+} $3d_{5/2}$	Rh$^+$ $3d_{3/2}$	Rh^{2+} $3d_{3/2}$
1	309.53 (1.58)		314.22 (1.71)	
2	309.34 (1.47)	310.56 (1.97)	314.01 (1.74)	315.40 (2.20)
3	309.35 (1.61)		314.04 (1.98)	

[a]Full-width at half-maximum (fwhm) values for peaks are given in parentheses. [b]These value were corrected against the C 1s peak using a value of 284.6 eV.

deconvolution using a Gaussian−Lorentian line shape fit. However, the compound **3** exhibits sharp Rh $3d_{5/2}$ and $3d_{3/2}$ peaks that agree well with those of **1**, indicating that the oxidation state of the rhodium atom is a rhodium(I); therefore, **3** in its RT phase is characterized as a rhodium(I)−semiquinonato complex.

X-ray Crystal Structure Analyses. The structures of the compound **3** were determined by X-ray crystallographic analyses, and the 1D chain structures in the RT and LT phases are shown in Figure 3. Both phases belong to the same monoclinic space group $P2_1/n$, and the asymmetric unit comprises two crystallographically independent complex molecules. A first-order phase transition generally occurs with symmetry breaking; however, although the compound **3** did not undergo such symmetry breaking, a drastic structural change has occurred. As shown in Figure S2, remarkable increases in the temperature dependence of the lattice parameters were observed to accompany the first-order phase transition. The crystal structure of **3** comprises of neutral 1D chains of the complex molecules stacked in a staggered arrangement along the a-axis, where the twisting angle between adjacent molecules estimated form the torsion angles of O1−Rh1−Rh2−O8 and O2−Rh1−Rh2−O7 is ca. 139° at 226 K in the RT phase. The Rh1−Rh2 and Rh1−Rh2* distances at 226 K are 3.0796(4) and 3.1045(4) Å, respectively, which are 0.186 Å shorter than those of $[Rh^I(3,6\text{-}DBSQ)(CO)_2]_\infty$ (**1**) (3.252(4) and 3.304(5) Å at 294−297 K)[35] and 0.21 Å longer than those of $[Rh^{I,II}(3,6\text{-}DBDiox\text{-}4,5\text{-}Cl_2)(CO)_2]_\infty$ (**2**) (2.8629(2)−2.8984(3) Å at 302 K) on average.[40] With respect to the intermolecular contacts in the 1D chain, five types of intermolecular C···O contact distances shorter than the sum of the van der Waals radii of contacting atoms (3.22 Å) exist between the carbon atoms of the semiquinonato ligands and the oxygen atoms of carbonyl ligands in the adjacent stacked molecules (3.113(4)−3.147(4) Å); they are represented by dashed lines in Figure 3a. The C−O distances in dioxolene ligands are known to reflect their oxidation states: 1.29(1) Å for the semiquinonate state and 1.35(1) Å for the catecholate state.[44] In the compound **3**, the average C−O distance is 1.311(3) Å; moreover, the six-membered rings of the coordinated dioxolene ligands exhibit a typical quinoid-type distortion: an average of 1.374(3) Å for two alternating short C−C bonds and an average of 1.433(7) Å for four longer C−C bonds. These structural features indicate that the electronic structure of the dioxolene ligands is considered to be a semiquinonate state; therefore, **3** consists of a diamagnetic rhodium(I) ion and a semiquinonate radical anion, in agreement with the result of our XPS measurements. The t-butyl group bonded to the C6 atom is disordered over two positions. On the other hand, the Rh1−Rh2 and Rh1−Rh2* distances at 162 K in the LT phase are 3.0426(7) and 3.0151(7) Å, respectively, which are shortened by ca. 0.037 and 0.090 Å, respectively, compared with those at 226 K. This observation indicates that the order of the shorter and longer Rh−Rh distances in the 1D chain is swapped during the first-order phase transition. With respect to the intermolecular contacts in the 1D chain in the LT phase, nine types of intermolecular C···O contacts shorter than the sum of the van der Waals radii of contacting atoms exist between the semiquinonato and the carbonyl ligands in the neighboring stacked molecules (3.001(6)−3.166(6) Å); they are represented by dashed lines in Figure 3c. The average C−O distance in the coordinated semiquinonato ligand is 1.316(9) Å, and the

7028

dx.doi.org/10.1021/ja5017014 | J. Am. Chem. Soc. 2014, 136, 7026−7037
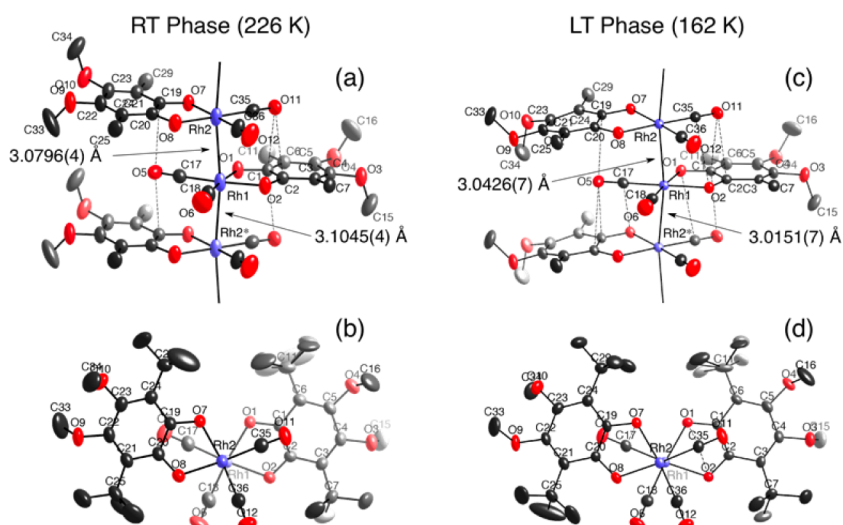
Figure 3. Crystal structures of [Rh(3,6-DBSQ-4,5-(MeO)$_2$)(CO)$_2$]$_\infty$ (**3**). (a) Structure of an infinite chain built from Rh···Rh interactions, and (b) a structural view along the Rh−Rh axis, showing an overlap mode of the complex molecules in the RT phase (226 K). Symmetry operation: * −1 + x, y, z. Five types of intermolecular C···O contact distances (3.113(4)−3.147(4) Å) shorter than the sum of the van der Waals radii of contacting atoms (3.22 Å) are represented by dashed lines. (c) Structure of an infinite chain, and (d) a structural view along the Rh−Rh axis in the LT phase (162 K). Nine types of intermolecular C···O contacts (3.001(6)−3.166(6) Å) are represented by dashed lines. Methyl carbon atoms of t-Bu groups are omitted for clarity in (a) and (c).
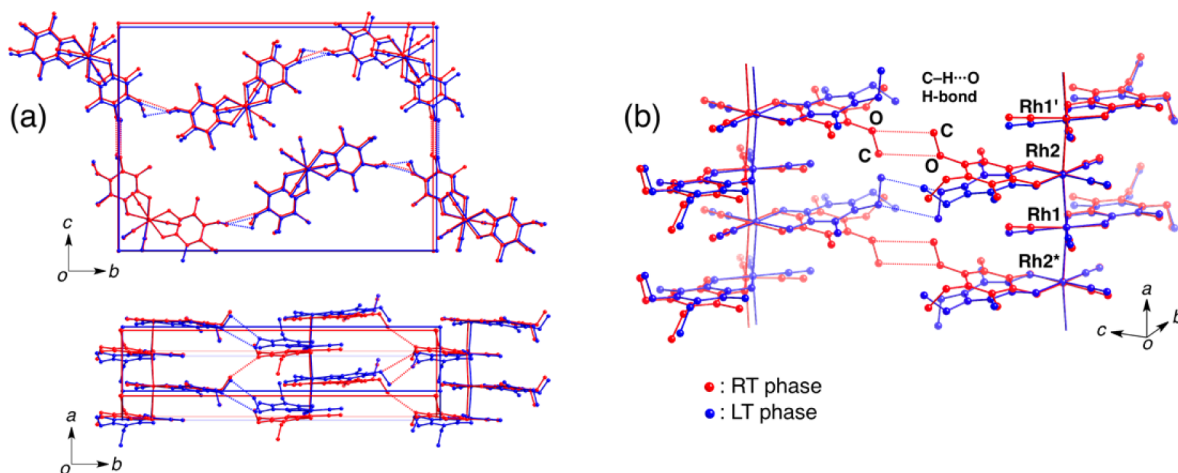
Figure 4. Comparison of the crystal structures in the RT (226 K) and LT (162 K) phases. (a) Superimposed drawing of the crystal structures in the RT and LT phases shown as red (RT phase) and blue (LT phase) ball-and-stick models by the overlapping of the origins of the two crystal lattices. In the c-axis drawing, the second layers of molecules are omitted for clarity. (b) Superimposed drawing of the 1D chains in the RT and LT phases shown as red (RT phase) and blue (LT phase) ball-and-stick models by the overlapping of both of the Rh1 atoms. (a, b) Dotted lines represent the intermolecular C−H···O hydrogen bonds between the adjacent methoxy groups; the methyl carbon atoms of t-Bu groups are omitted for clarity.

six-membered rings also show a quinoid-type distortion: an average of 1.383(8) Å for two alternating short C−C bonds and an average of 1.434(8) Å for four longer C−C bonds. Therefore, **3**, in its LT phase, is also characterized as a rhodium(I)−semiquinonato complex. The disorder of the t-butyl group observed in the RT phase is maintained in the LT phase.

To clarify the origin of the first-order phase transition observed at 223.5 K during heating, a superimposed drawing of crystal structures with the origins of the crystal lattices overlapped is presented in Figure 4a. In general, the hydrogen bond is judged to exist when the distance between the proton donor and the acceptor atoms is less than the sum of the van der Waals radii of those atoms (C···O = 3.22 Å).[45] However, the C···O contacts with distances that range from 3.0 to 3.8 Å

are judged as weak hydrogen bonds because such contacts may affect the molecular geometry and crystal packing.[46] In the compound **3**, the C···O distances between the methoxy groups of the adjacent 1D chains are relatively short. These distances in the RT and LT phases are in the range of 3.465−3.654 Å and 3.562−3.679 Å, respectively, indicating the presence of weak C−H···O hydrogen bonds, as per the above-mentioned criterion. As a result, the 1D chains are connected three dimensionally by the weak C−H···O hydrogen bonds, as shown in Figure 4a. The most important feature of the first-order phase transition is that an unusual exchange of hydrogen-bonding partners occurs during the phase transition. As shown in Figure 4b, the semiquinonato ligand coordinated to an Rh2 atom in the RT phase is warped out from a RhO$_2$C$_2$ plane by ca. 6°, whereas the direction of the warp of the semiquinonato

ligand and the orientation of two methoxy groups of the same ligand are inverted in the LT phase. Therefore, this abnormal structural change observed for the semiquinonato ligand is related to the drastic rearrangement of the hydrogen-bonding pattern during the phase transition. With respect to another striking difference between the crystal structures in the RT and LT phases, as seen in Figure 3a, the temperature factors of the rhodium atoms and its surrounding oxygen and carbon atoms in the RT phase are extended in the 1D chain direction, suggesting the possibility of positional disorder or vibration with a large amplitude for these atoms.

Magnetic Properties. Temperature dependence of the molar magnetic susceptibility (χ_M) and the product of the magnetic susceptibility and temperature ($\chi_M T$) are shown in Figures S3 and 5, respectively. The compound **3** exhibits a
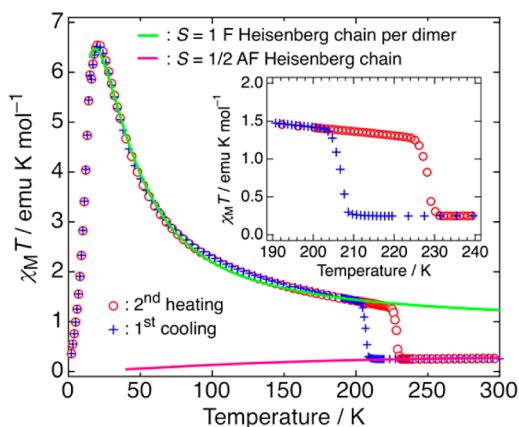

Figure 5. Temperature dependence of the product of the molar magnetic susceptibility and temperature ($\chi_M T$). Data were measured on a polycrystalline sample under an applied magnetic field of 200 Oe. The solid lines represent the least-squares fits of the data with the models described in the text.

drastic change in magnetic behavior with thermal hysteresis between 228 and 207 K; this behavior is consistent with the result of the DSC measurement (Figure S1). The $\chi_M T$ value at 300 K is 0.254 emu K mol^{-1}, which is only two-thirds the spin-only value of $S = 1/2$ (0.375 emu K mol^{-1}) and slightly decreases to 0.250 emu K mol^{-1} when the temperature is decreased to 217 K. To evaluate the magnetic interactions in the RT phase, we tentatively analyzed the magnetic data of **3** using a theoretical equation for the $S = 1/2$ antiferromagnetic (AF) Heisenberg chain model (Bonner−Fisher equation, $H = -J \Sigma S_i \cdot S_{i+1}$).[47] Details about the fittings using other theoretical models with $S = 1/2$ are described in Figure S4.[48,49] The best-fit parameters obtained in the temperature range of 300−214 K are $J/k_B = -163(3)$ K with g fixed at 2.00 expected for organic radicals. As will be discussed in the DFT Calculations section, it is considered that the theoretical equations cannot reproduce the experimental magnetic data well because the next-nearest-neighbor interactions are relatively large but are not taken into consideration in the theoretical equations.

An abrupt increase in the $\chi_M T$ value with thermal hysteresis was observed with the first-order phase transition (Figure 5). In the LT phase, the $\chi_M T$ value drastically increases to 6.51 emu K mol^{-1} when the temperature is decreased to 20 K and then rapidly decreases. Surprisingly, magnetic anisotropy of which the easy axis of magnetization is parallel to the 1D chain direction is observed in the LT phase (Figures S5 and S6). This

magnetic anisotropy is attributable to the contribution of d orbitals of rhodium ions since the orbital angular momentum of organic radicals is generally disappeared. The observed drastic increase in the $\chi_M T$ value indicates the presence of a very strong ferromagnetic interaction operating between the spins in the 1D chain. We attempted to tentatively analyze the magnetic data for the LT phase using the $S = 1/2$ ferromagnetic (F) Heisenberg uniform chain model (Baker equation)[50] because no theoretical equation is available for an $S = 1/2$ ferromagnetic alternating chain model. However, our attempts were unsuccessful because the experimental data deviate from the theoretical values toward higher values with decreasing temperature (Figure S7). Therefore, to assess the magnetic interaction, we used, as a first approximation, the half-value of the $S = 1$ ferromagnetic (F) Heisenberg chain model with the Hamiltonian $H = -J \Sigma S_i \cdot S_{i+1}$ by assuming that the alternately stacked neighboring complex molecules in the 1D chain form triplet dimers via a very strong ferromagnetic interaction.[51] In addition, the mean-field approximation with zJ' was applied to the analysis to compensate for the antiferromagnetic interaction between chains.[52] The least-squares fit of this model to the experimental data at temperatures greater than 17 K resulted in $J/k_B = +74(1)$ K, $g = 2.67(2)$, and $zJ'/k_B = -1.98(3)$ K, respectively, where the g factor is included in the least-squares fit considering the magnetic anisotropy. These results indicate that the adjacent molecules situated alternately in the chain are considered to form the triplet dimers because of extremely strong ferromagnetic interaction and that the magnetic interaction between them is also ferromagnetic. The small negative value of zJ'/k_B indicates that antiferromagnetic interactions operate between the ferromagnetic 1D chains.

To investigate the nature of magnetic ordering processes at LT in detail, we performed ac magnetic measurements in an ac field of 2 Oe oscillating at 1−997 Hz. The in-phase component of the ac susceptibility, χ', exhibits a round maximum at ca. 16 K, as represented by the dotted curve in Figure 6. However, the corresponding out-of-phase χ'' component is absent, clearly
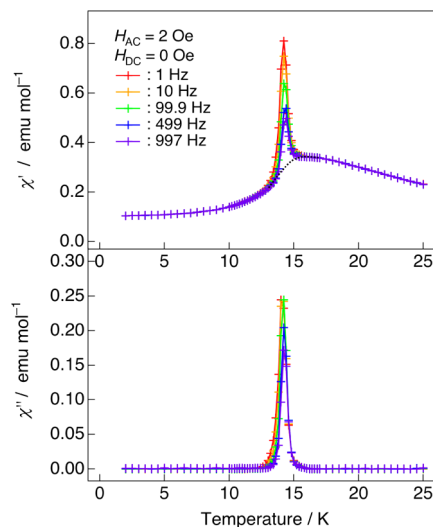
Figure 6. In-phase (χ') and out-of-phase (χ'') ac susceptibility as a function of temperature. Ac magnetic measurements were performed on a polycrystalline sample in an ac field of 2 Oe oscillating at 1−997 Hz with a dc bias field of zero. The round maximum at ca. 16 K observed for the in-phase component of the ac susceptibility, χ', is represented by a dotted curve.

indicating antiferromagnetic coupling between the ferromagnetic 1D chains. Furthermore, the frequency dependence of the intensity of the in-phase component χ' and that of the nonzero out-of-phase component χ'' start to appear simultaneously at temperature below 16.4 K. Then, the compound **3** exhibits sharp peaks in the both χ' and χ'' components at 14.2 and 14.0 K, respectively. The appearance of the net magnetic moment in the antiferromagnetic state is attributed to the imperfect cancellation of the antiferromagnetically coupled spins between the ferromagnetic 1D chains because of spin canting, which is the so-called weak ferromagnetism.[53−55] In general, the critical temperature for the onset of spontaneous magnetization can be defined as the temperature at which the χ' component shows a maximum and the χ'' component starts to appear. However, for the compound **3**, the rapid increase in χ' and χ'' that started at temperature below 16.4 K is attributed to the rapid development of ferromagnetic-like correlation length; moreover, the sharp peaks in both the χ' and χ'' components are due to spontaneous magnetization that originates from the 3D magnetic ordering of the net magnetic moments. Therefore, the transition temperature (T_N) was determined to be 14.2 K on the basis of the peak temperature of χ'. Generally, spin canting is known to arise from the magnetic anisotropy and/or the antisymmetric magnetic exchange (Dzyaloshinsky−Moriya interaction), which requires the lack of inversion symmetry between magnetic centers.[53,56,57] The plots of $\ln(\chi T)$ vs $1/T$ for both the ac and dc measurement data exhibits a linear part (Figure S8), suggesting the possibility of anisotropic Heisenberg or Ising-like 1D behavior, which is consistent with the observed magnetic anisotropy.[58,59] Given the structural feature without an inversion center between the complex molecules, the Dzyaloshinsky−Moriya interaction should also be considered as a possible source of spin canting. Thus, the observed spin canting is considered to be due to the magnetic anisotropy and/or the Dzyaloshinsky−Moriya interaction.

Figures 7 and S9 show the field dependence of magnetization M measured at 2 K on a polycrystalline sample. The M vs H curve shows a double sigmoidal shape that originates from the field-induced spin-flop transition from an antiferromagnetic state between neighboring ferromagnetic chains to a ferromagnetic state with hysteresis, which is characteristic of a metamagnet.[60] The critical field is estimated to be $H_c = 3.25$
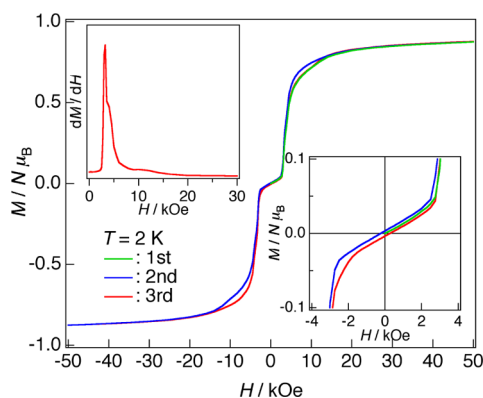
Figure 7. Field dependence of magnetization M measured on a polycrystalline sample at 2 K. The inset in the upper-left corner shows the field dependence of differential magnetization dM/dH. The dM/dH vs H curve shows a peak at 3.25 kOe, which corresponds to the critical field (H_c). The inset in the lower-right corner is an enlarged view that shows the small hysteresis loop between +3 and −3 kOe.

kOe on the basis of the maximum in the dM/dH vs H curve. The magnetization value at an applied field of 50 kOe is 0.877 $N\mu_B$, which is smaller than the saturation magnetization (M_s) of 1.0 $N\mu_B$ expected for $S = 1/2$ with $g = 2.00$. The magnetization deficit is due to the magnetic anisotropy observed for the aligned needle-shaped crystals (Figure S10). Whereas, in the low-field region, a very small magnetic hysteresis loop is observed with a coercive field of 255 Oe and a remnant magnetization (M_r) of 0.0035 $N\mu_B$, which coincides with the appearance of spontaneous magnetization because of the spin canting (Figure S11).

As already described, the magnetic interaction in **3** changes from antiferromagnetic to strongly ferromagnetic upon shrinkage of the 1D chain, which occurs during the first-order phase transition (*a* axis in Figure S2). Therefore, we measured the magnetic susceptibility under applied pressures because the magnetic response that occurs when the Rh−Rh distances physically shrink by the application of pressure is very interesting; the results obtained are shown in Figure 8. The
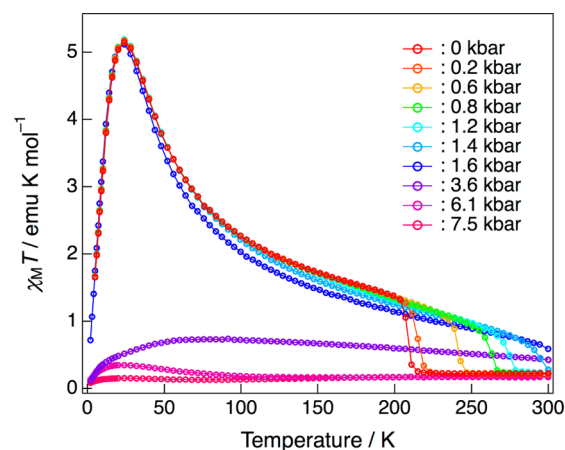

Figure 8. Temperature dependence of molar magnetic susceptibility in the form of $\chi_M T$ vs T plots for $[Rh(3,6\text{-DBSQ-}4,5\text{-}(MeO)_2)(CO)_2]_\infty$ (**3**) measured on a polycrystalline sample under an applied magnetic field of 10 kOe and under several hydrostatic pressures up to 7.5 kbar. Each measurement was performed during a cooling process.

ferromagnetic LT phase is stabilized up to RT by the application of a relatively weak pressure of 1.4 kbar, under which the first-order phase transition temperatures increase linearly with increasing applied pressure (Figure S12). The drastic change in the first-order phase-transition temperature induced by a small perturbation is considered to reflect its bistable character. Furthermore, under the pressure higher than 3.6 kbar, the compound **3** underwent a phase transition to another phase, at which the strong ferromagnetic interaction disappeared. The most probable origin of the phase transition will be discussed on the basis of the results of DFT calculations in the next section. The observed pressure dependences of the magnetic susceptibility were reversible.

DFT Calculations. To better understand the electronic structure and origin of the ferromagnetic interaction in the 1D chain, we performed density functional theory (DFT) calculations based on the monomer, dimer, and trimer models constructed using the atomic coordinates of the ferromagnetic LT phase (Figures 9 and S13). The frontier orbitals of these models are shown in Figures S14−S16, and their energy diagram is shown in Figure 10. First, the singly occupied
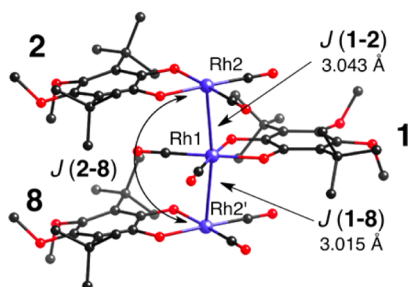
Figure 9. Trimer model for DFT calculations using the atomic coordinates of the ferromagnetic LT phase.
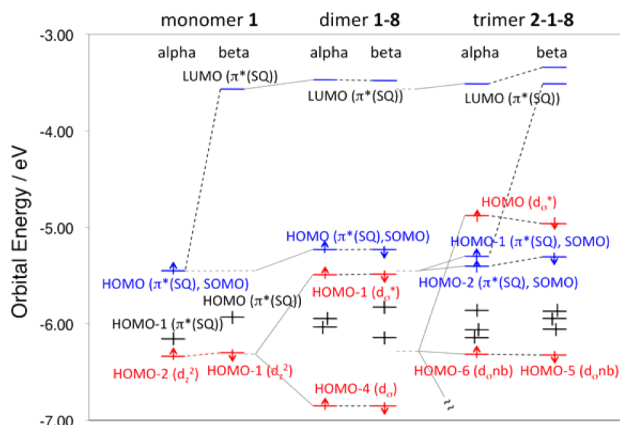
Figure 10. Energy-level diagram of the frontier molecular orbitals for the monomer **1**, dimer **1-8**, and trimer **2-1-8** models derived from UB3LYP calculations. The MIDI + polarization function, 6-31G*, and 6-31+G* basis functions were used for Rh atoms, 3,6-DBSQ-4,5-(MeO)$_2$ ligand, and CO ligands, respectively. All calculations were performed using Gaussian 09.[61]

molecular orbital (SOMO) of monomer model **1** is derived from the π^* orbital of the 3,6-DBSQ-4,5-(MeO)$_2$ radical ligand, which is delocalized over the entire molecule as shown in Figure 11. Consideration of how the spin of the SOMO is
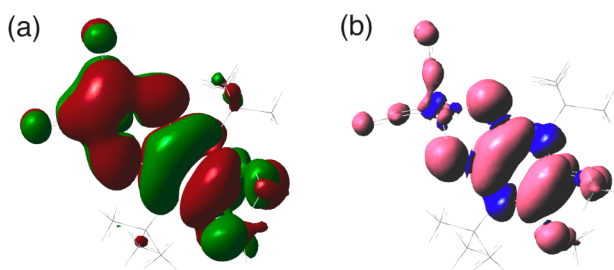
Figure 11. (a) Singly occupied natural orbital (threshold = 0.01) and (b) the spin-density isosurface (threshold = 0.0005) of monomer model **1** derived from UB3LYP calculations.

spread inside the monomer is important, and the spin density in the compound **3** is also delocalized not only toward the rhodium atom but also toward the carbonyl ligands. The magnetic orbital is considered to expand in this manner because the symmetry and energy levels of the molecular orbitals of the 3,6-DBSQ-4,5-(MeO)$_2$ and CO ligands would compromise well. The energy level of the d$_{z^2}$ orbital that primarily contributes to electrical conductivity in the solid state is −0.9 eV lower than the α-SOMO level. The lowest unoccupied molecular orbitals (LUMO) is predominantly a semiquinonato

π^* orbital (90%), with some contributions from a Rh 4d orbital and carbonyl ligands. Second, in the dimer model **1-8**, the highest occupied molecular orbitals (HOMOs) primarily comprise a semiquinonato π^* orbital (52%), with a significant admixture of a dσ^* orbital (40%) coming from axial Rh 4d$_{z^2}$ orbitals, and its energy levels are not substantially changed compared with that of the monomer. In contrast, the HOMO−1s primarily comprise a dσ^* orbital (55%), with considerable contribution from a π^* orbital (37%); moreover, the dσ^* orbital is significantly destabilized because of a strong σ^* interaction between the 4d$_{z^2}$ orbitals due to the significantly short Rh−Rh distances. The energies of the HOMOs and HOMO−1s are similar ($\Delta E \approx 0.25$ eV), indicating the pseudodegeneracy of these orbitals. The HOMO−LUMO gap is 1.76 eV. Third, in the trimer model **2-1-8**, the dσ^* orbital with a large overlap of the d$_{z^2}$ orbitals is further destabilized because of the strong σ^* Rh−Rh interaction, leading to the HOMO. In contrast, the energy levels of the semiquinonato π^* orbitals are almost unchanged due to lack of direct interactions among them, resulting in the HOMO−1 and HOMO−2, i.e., the interesting SOMO−HOMO energy-level conversion has occurred, and the HOMO−LUMO gap is decreased to 1.37 eV. Hence, on the basis of these results, the 1D d band formed from the d$_{z^2}$ orbitals in the solid state is expected to further expand due to the effect of the 1D chain, leading to a further approach of the upper levels of the filled d band to the LUMO levels composed of the vacant π^* orbitals. As a possible explanation of the origin of the phase transition observed in the magnetic susceptibility under applied pressures above 3.6 kbar, the upper levels of the d band can be considered to interact with the LUMO levels as the Rh−Rh distance decreases under the applied pressure. This interaction would lead to the mixed-valence state due to the charge transfer from the filled d band to vacant π^* orbitals because the application of pressure primarily results in a decrease in the Rh−Rh distance.

To estimate the effective exchange integral J, we calculated the energies of the high-spin (HS) triplet state and the low-spin (LS) spin-singlet state of the dimer units in the intra- and interchains using the unrestricted hybrid functional DFT method (UB3LYP).[62] The arrangements of the complex molecules used in the calculation are shown in Figure S13, and the results are listed in Table S2. The effective exchange integrals J_{ab}/k_B of the models **1-8** (Rh−Rh = 3.015 Å) and **1-2** (Rh−Rh = 3.043 Å) estimated from these energy values on the basis of the following equation were −832.7 and −749.1 K, respectively, which suggests that the intrachain magnetic interaction is strongly antiferromagnetic rather than ferromagnetic:

$$H = -\sum_{a,b} J_{ab} S_a \cdot S_b$$

$$J_{ab} = \frac{E^{LS} - E^{HS}}{2(\langle S^2 \rangle^{HS} - \langle S^2 \rangle^{LS})}$$

where E^X and $\langle S^2 \rangle^X$ represent the total energies and the $\langle S^2 \rangle$ values of the spin state X (X = HS or LS), respectively. The estimated J values, however, are in good agreement with that observed for a rhodium(I)−semiquinonato dimer complex, [Rh(3,6-DBSQ-4,5-(2R,4R-PDO))(CO)$_2$]$_2$[Rh(3,6-DBSQ-4,5-(2S,4S)-PDO)](CO)$_2$]$_2$ (Rh−Rh = 3.0469(7) Å at 150 K, J/k_B = −755 K), where 3,6-DBSQ-4,5-(2R,4R)-PDO and 3,6-DBSQ-4,5-(2S,4S)-PDO represent the 2R,4R- and 2S,4S-

forms of 3,6-di-*tert*-butyl-4,5-(2,4)-pentanedioxy-1,2-benzose-miquinonato (unpublished results by our group). On the other hand, the J_{ab} values of the models **1-4** and **3-4** shown in Figure S13 were calculated to −0.5 and −0.6 K, respectively, in which the monomeric complexes are connected by the CH···O hydrogen bonds; these values are consistent with the observed antiferromagnetic interchain interaction. We subsequently introduced the trimer model **2-1-8**, as shown in Figure 9, to consider the delocalization effects of the magnetic orbitals over the Rh−Rh axis direction because the dimer models can only take nearest-neighbor interactions into consideration. The effective exchange integrals J(**1-2**), J(**1-8**), and J(**2-8**) for the each spin state were calculated by DFT energies using an algorithm to obtain the J values of multispin systems,[63] and the results obtained are listed in Table 2. The J(**1-2**)/k_B and J(**1-**

Table 2. Calculated Effective Exchange Integral J/k_B of the Trimer Model Using the Atomic Coordinates of the Ferromagnetic LT Phase

spin state of model **2-1-8**	total energy, au	J	J/k_B, K
(↑↑↑)	−17507.586080	J (2-8)	−200.1
(↓↑↑)	−17507.587200	J (1-2)	−478.1
(↑↑↓)	−17507.587243	J (1-8)	−512.2
(↑↓↑)	−17507.587710		

8)/k_B values are −478.1 and −512.2 K, which are smaller than those of the dimer model, and it is found that the delocalization effect of the orbitals is quite large. Furthermore, the J(**2-8**) value is too large to be ignored, indicating that the magnetic interaction is extended over a long range. Notably, the negative value of the J(**2-8**) value suggests that a certain fluctuation would occur. However, the ferromagnetic interaction could not be reproduced, even in the trimer model. To examine the J_{ab} value of only the SOMO−SOMO component in the model **1-8** (Rh−Rh = 3.015 Å), the CASCI [2,2] method was performed using the previously described DFT natural orbitals.[64] As a result, the J_{ab}/k_B value was estimated to be +320.6 K, and the magnetic interaction for only the SOMO−SOMO component can reproduce the ferromagnetic interaction (Figure S17). Because the DFT calculation of the dimer model was able to reproduce the J value observed for the dimer complex, the spin state of the polymer complex **3** is considered to be completely different from that of the dimer complex. To reproduce the ferromagnetic interaction using the UB3LYP method, we considered that a model calculation that includes many more molecules would be required, although such a calculation becomes very difficult.

Electronic Absorption Spectra. The UV−vis−NIR−mid-IR spectrum of **3** is shown in Figure 12, together with the spectra of **1** and **2,** and the spectral data are summarized in Table S3. The dominant feature of the spectra of **1**−**3** is an intense broad electronic absorption ranging from the NIR to the mid-IR region; this band is absent from their CH$_2$Cl$_2$ solution spectra. On the basis of the results of the DFT calculations for **3**, the broad absorption bands observed for **1** and **3**, which exhibit absorption maxima of 6700 and 6550 cm^{-1}, respectively, can be attributed to the charge-transfer absorption from a 1D d band resulting from axial d$_{z^2}$ orbitals to vacant semiquinonato π* levels. However, the broad absorption band of **2** is considered to consist of several overlapping bands, including the intervalence charge-transfer transitions of Rh^{2+} ← Rh$^+$ and/or π*(SQ) ← π*(Cat^{2-}), together with the above-
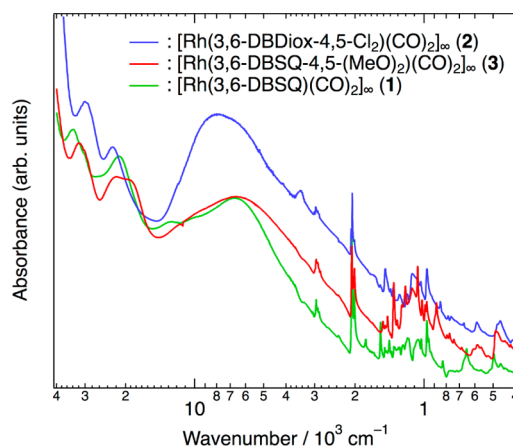
Figure 12. UV−vis−NIR−mid-IR spectrum of [Rh(3,6-DBSQ-4,5-(MeO)$_2$)(CO)$_2$]$_\infty$ (**3**) in the solid state (KBr pressed disk), together with those of [Rh^I(3,6-DBSQ)(CO)$_2$]$_\infty$ (**1**) and [Rh^{I,III}(3,6-DBDiox-4,5-Cl$_2$)(CO)$_2$]$_\infty$ (**2**). The UV−vis−NIR and mid-IR spectra were connected smoothly at ~4000−5000 cm^{-1}.

mentioned π*(SQ) ← 1D d-band (d$_{z^2}$) transition.[40] Although the broad absorption maximum is not directly related to a HOMO−LUMO gap, the electronic absorbance is known to be proportional to $D_J \mu^2$, where D_J is the joint density of state and μ is the transition dipole.[65] As the more the absorption band extends further from mid- to far-IR region, the energy of the electronic excitations decreases, which leads to high electrical conductivity. Consistent with this observation, the compound **2**, which exhibits remarkably strong electronic absorption in the low-energy region, exhibits a substantial electrical conductivity of 17−34 S cm^{-1} at RT.[40] The compound **3**, which exhibits a large expanse of the electronic absorption band in the mid-IR region compared to that of **1**, is expected to demonstrate relatively high electrical conductivity, although the absorption maxima of **1** and **3** are approximately the same.

Electrical Properties. As shown in Figure 13, the temperature dependence of the electrical resistivity ρ shows a clear hysteresis that coincides with the first-order phase transition, demonstrating that the present compound exhibits bistability with respect to its magnetic and conductive
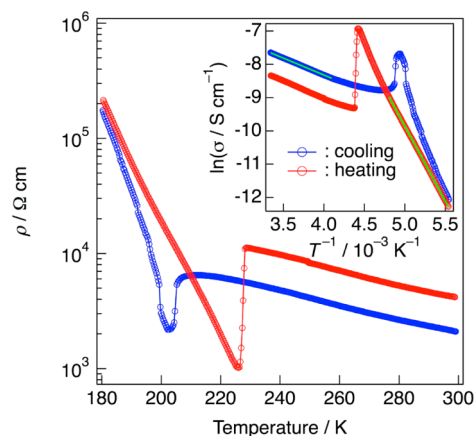
Figure 13. Temperature dependence of the electrical resistivity ρ and the electrical conductivity σ measured along the chain axis, *a*. The disagreement between the resistivities in the RT phase measured in the cooling and heating processes is attributable to microcracks that develop during the first-order phase transition.

properties. As expected from analysis of its electronic absorption spectrum, the compound **3** shows a relatively high electrical conductivity of 4.8×10^{-4} S cm^{-1} at RT despite Rh not being in a mixed-valence state. This relatively high conductivity can be attributed to the reduction of the energy gap between the upper level of the filled 1D d band and the vacant semiquinonato π^* levels because of the remarkable expanse of the d band due to the strong Rh−Rh interactions. The activation energies E_a in the RT and LT phases, as estimated from the Arrhenius plot, are 88 meV ($T = 300-244$ K) and 386 meV ($T = 209-181$ K), respectively. As an important difference between these phases, the thermal ellipsoids of the rhodium and its neighboring coordinated atoms in the RT phase are unusually elongated in the 1D chain direction as can be seen in Figure 3. This is considered to occur due to large-amplitude vibrations in 1D chain direction rather than positional disorder because this behavior appeared only in the RT phase. When a Rh−Rh distance shrinks largely accompanying the large-amplitude vibration, the d band becomes wider and its upper levels are expected to further approach the vacant π^* orbitals. Therefore, it is expected that the electron excitation becomes easy with the shrinkage of Rh−Rh distance, thus leading to the relatively small activation energy observed in the RT phase. Unfortunately, the giant negative magnetoresistance expected for a magnetic conductor was not observed for the compound **3** (Figure S18).[66,67]

CONCLUSIONS

Herein, we described a 1D single-component molecular system based on a rhodium(I)−semiquinonato complex that exhibits a unique bistable multifunctionality with respect to its magnetic and conductive properties. The observed bistability is due to a thermal hysteresis across a first-order phase transition that accompanies the exchange of the interchain C−H···O hydrogen-bond partners between the semiquinonato ligands. The strong overlaps of complex molecules lead to strong ferromagnetic interactions in the LT phase; moreover, the magnetic interactions in the 1D chain drastically change from strongly ferromagnetic in the LT phase to antiferromagnetic in the RT phase with the hysteresis. DFT calculations for the dimer and trimer models could not reproduce the strong ferromagnetic interaction observed for the compound **3**; however, the result for the dimer model is consistent with the large negative J value observed for a dimer complex. Therefore, the spin state of the coordination polymer **3** is considered to be completely different from that of the dimer complex. The reproduction of the very strong ferromagnetic interaction of **3** by theoretical calculation is an important future issue to understand the electronic structure of this type of coordination polymer. The electrical conductivity at 300 K is 4.8×10^{-4} S cm^{-1}, which is relatively high despite Rh not being in a mixed-valence state. This relatively high conductivity can be attributed to the reduction of the energy gap between the upper level of the filled 1D d band and the vacant semiquinonato π^* levels because of the remarkable expanse of the d band due to the strong Rh−Rh interactions. The temperature dependence of electrical resistivity also demonstrates a clear hysteresis across the first-order phase transition, indicating that the present compound exhibits bistability with respect to its magnetic and conductive properties. Reflecting a characteristic of the bistability, the ferromagnetic LT phase can be easily stabilized up to RT by the application of a relatively weak pressure of 1.4 kbar, thereby demonstrating that

simultaneous control of the multifunctionality through external perturbation is possible.

The nature for the remarkable difference in the electronic states in the RT and LT phases could not be explained clearly on the basis of our experimental results. However, unusually elongated thermal ellipsoids of the rhodium and its neighboring coordinated atoms observed in the RT phase suggest large-amplitude vibrations of these atoms in 1D chain direction. Such vibrations are expected to affect the striking difference between the electronic states of these phases through vibronic interactions;[68] we therefore intend to verify this hypothesis in the future. Unfortunately, the expected giant negative magnetoresistance due to the synergy between electrical conductivity and magnetic interactions expected for a magnetic conductor was not observed for the compound **3**.[66,67] To exhibit giant magnetoresistance, the compound should exhibit a highly conductive or metallic state at low temperatures, at which the localized spins are easily arranged by an applied magnetic field. Thus, efforts to develop a 1D mixed-valence rhodium(I,II)−semiquinonato/catecholato complex that exhibits both ferromagnetic interactions and metallic conduction through control of the frontier molecular orbitals via chemical modification are now in progress.

EXPERIMENTAL SECTION

Syntheses. All syntheses were performed at RT under an argon atmosphere using standard vacuum-line and Schlenk techniques. All solvents were dried using appropriate drying agents and were freshly distilled under argon before use.[69] Dodecacarbonyltetrarhodium(0) ($[Rh_4(CO)_{12}]$),[70] 3,6-di-*tert*-butyl-1,2-benzoquinone (3,6-DBBQ), 3,6-di-*tert*-butyl-4,5-dimethoxy-1,2-benzoquinone (3,6-DBBQ-4,5-$(MeO)_2$),[71] and $[Rh^{I,II}(3,6\text{-DBDiox-4,5-Cl}_2)(CO)_2]_\infty$ (**2**)[40] were prepared according to published procedures. Elemental analyses were performed at the Center for Organic Elemental Microanalysis of the Graduate School of Pharmaceutical Sciences, Kyoto University.

Synthesis of $[Rh(3,6\text{-DBSQ})(CO)_2]_\infty$ *(**1**).* Nevodchikov et al. reported the synthesis of compound **1** by the reaction of Tl(3,6-DBSQ) with $[RhCl(CO)_2]_2$ in toluene.[36] However, we prepared the compound **1** using our developed redox reaction of $[Rh_4(CO)_{12}]$ with the corresponding benzoquinone derivative because the disposal of thallium waste is expensive.[72] $[Rh_4(CO)_{12}]$ (56.0 mg, 74.9 μmol) and 3,6-DBBQ (69.0 mg, 313 μmol) were placed in a small glass container (10 mm i.d., 25 mm height) and a large glass sealable container (16.5 mm i.d., 40 mm height), respectively; subsequently, the small glass container was placed inside the large sealable container such that 3,6-DBBQ was not buried under the small container. After filling the glass sealable container with dry pentane, well-shaped black needle-like crystals of **1** were obtained within 2 weeks by slow diffusion of $[Rh_4(CO)_{12}]$ and 3,6-DBBQ. The resulting black crystals were collected by suction filtration and were rinsed with ice-cooled pentane. Yield: 61 mg (54%). Elemental analysis: calculated for $C_{16}H_{20}O_4Rh$: C, 50.67; H, 5.32%. Found: C, 50.58; H, 5.27%.

Synthesis of $[Rh(3,6\text{-DBSQ-}(MeO)_2)(CO)_2]_\infty$ *(**3**).* Compound **3** was also obtained by a redox reaction of $[Rh_4(CO)_{12}]$ with the corresponding benzoquinone derivative in pentane as follows:[72] $[Rh_4(CO)_{12}]$ (56.9 mg, 76.1 μmol) and 3,6-DBBQ-4,5-$(MeO)_2$ (85.17 mg, 304 μmol) were dissolved in dry pentane (11.5 mL) at 35 °C. The solution was maintained at 35 °C for 10 min with stirring and was subsequently filtered using a PTFE cannula equipped with a glass-fiber filter. The filtrate was then gradually cooled to −20 °C for 20 h using a refrigerated thermostatic bath. The resulting dark-brown needle-like crystals were collected by suction filtration and were rinsed with ice-cooled pentane. Yield: 38 mg (28%). Elemental analysis: calculated for $C_{18}H_{24}O_6Rh$: C, 49.22; H, 5.51; O, 21.85%. Found: C, 48.94; H, 5.58; O, 22.02%.

X-ray Photoelectron Spectroscopy. XPS data were obtained on a VG ESCALAB 220i-XL spectrometer equipped with a non-

monochromatized MgKα radiation source (1253.6 eV) operated at 15 kV and 20 mA. Measurements were conducted in the 10^{-6} Pa pressure range. Samples were ground into powders and spread onto conductive adhesive tape attached to sample holders. The absence of X-ray beam effects was verified by the X-ray power dependence of the XPS spectra. The carbon 1s binding energy (284.6 eV) was used to calibrate the binding energies. Curve-fitting analysis was performed with the iterative least-squares computer program XPSPEAK41 using a combination of Gaussian and Lorentzian line shapes.

Calorimetry. DSC measurements were performed with a PerkinElmer Diamond DSC at a scanning rate of 10 K min^{-1} using helium as the purge gas. Heat-capacity measurements were performed in the temperature range of 12−300 K with a laboratory made LT adiabatic calorimeter for small samples.[42] The sample of 0.15374 g after buoyancy correction was loaded into a gold-plated copper cell and sealed under helium gas at ambient pressure using an indium gasket. The helium gas functions as a heat-exchange medium. Thermometry was performed with a rhodium−iron alloy resistance thermometer (nominal 27 Ω, Oxford Instruments) calibrated on the basis of the international temperature scale of 1990 (ITS-90).

X-ray Crystal Structure Analyses. Crystals of **3** were mounted on glass fibers using Apiezon grease. Single-crystal X-ray diffraction data for **3** were collected at 226 and 162 K using Mo Kα radiation of λ = 0.710 70 Å on a Rigaku AFC7 Mercury CCD diffractometer equipped with a Rigaku variable-temperature apparatus; the data were collected using a cold nitrogen gas stream method at the Instrument Center, Institute for Molecular Science. Data collection, cell refinements, indexing, peak integrations, and scaling of the diffraction data were performed using the CrystalClear software.[73] Lorentz, polarization, and numerical absorption corrections were applied to the intensity data. The structures were solved by direct methods (SIR97)[74] and expanded using Fourier techniques. All refinements were made on F^2 by a full-matrix least-squares method using the SHELXL-97 program.[75] The X-ray analyses were performed using the free GUI software Yadokari-XG 2009.[76,77] All non-hydrogen atoms in **3** were refined anisotropically, whereas hydrogen atoms on the methyl groups were placed in geometrically calculated positions and refined with temperature factors 1.5 times greater than those of their parent atoms. At 226 and 162 K, the *t*-butyl group bound to the C6 atom of the semiquinonato ligand coordinated to the Rh1 atom in each structure was observed to be disordered over two orientations, which were modeled with relative occupancies of 0.689(16) and 0.311(16) for the 226 K data and 0.459(15) and 0.541(15) for the 162 K data. Further details of the crystal data and crystal-structure refinements for **3** are available in the Supporting Information.

UV−vis−Near-IR and Mid-IR Spectroscopies. UV−vis−near-IR spectra of complexes **1**−**3** as KBr pressed disks were recorded on a Hitachi U-3500 spectrophotometer equipped with a 60 mm i.d. integrating sphere apparatus. IR spectra were recorded as KBr pressed disks on a JASCO FT/IR-4100 spectrophotometer.

Magnetic Measurements. Magnetic measurements were performed using a Quantum Design MPMS-5SH or MPMS-XL7 SQUID magnetometer. A polycrystalline sample (28.94 mg) of **3** held in a polyethylene film (20.05 mg) inside a plastic straw was used. Magnetic susceptibility measurements on the polycrystalline sample were performed from 300 to 2 K under an applied magnetic field of 200 Oe. Field dependence of magnetization on the polycrystalline sample was measured in magnetic fields from 0 to 50 kOe at 25, 15, 14.4, and 10 K and from −50 to 50 kOe at 2 K. The diamagnetic contributions of the polyethylene film and plastic straw were measured from 300 to 2 K under an applied magnetic field of 10 kOe, and the corresponding diamagnetic contribution obtained by multiplying the measured value by a factor of 200/10000 was subtracted from the raw data. The paramagnetic component of the molar magnetic susceptibility (χ_M) was obtained after subtraction of the calculated diamagnetic core contribution (-229.4×10^{-6} emu mol^{-1}) estimated from the measured diamagnetic susceptibility of 3,6-di-*tert*-butyl-4,5-dimethoxy-1,2-benzoquinone (3,6-DBBQ-4,5-(MeO)$_2$) (-169.4×10^{-6} emu mol^{-1}) and the Pascal's constants for a rhodium(0) atom and two carbon monoxide ligands. Ac measurements on the polycrystalline

sample were performed at frequencies of 1, 10, 99.9, 499, and 997 Hz with an ac field amplitude of 2 Oe with a zero dc bias field. The magnetic susceptibility on the aligned single crystals was measured in the temperature range of 300−2 K and in an applied magnetic field of 1 kOe using numerous needle crystals (0.70 mg) aligned on a plastic plate (ca. 5 × 4 mm^2) with Apiezon N grease inside a plastic straw. The magnetization on the aligned single crystals was measured in the range of −50 to 50 kOe at 2 K. The diamagnetic contributions of the sample holder and plastic straw were measured in the temperature range of 300−2 K under an applied magnetic field of 10 kOe, and the corresponding diamagnetic contribution obtained by multiplying the measured value by a factor of 1000/10000 was subtracted from the raw data. Magnetic measurements under various hydrostatic pressures up to 7.5 kbar were performed using a piston-cylinder type pressure cell constructed from Cu−Be alloy. The crystals (13.52 mg) were dispersed into a pressure-transmitting medium, Daphne 7373, with a piece of tin as the manometer in a Teflon bucket. Actual pressure was calibrated using the superconducting transition temperature of tin. The data under various pressures from 0 to 7.5 kbar were normalized by adjusting the magnetic susceptibility in the temperature range of 300−224 K measured at 0 kbar using the pressure cell to those measured inside a plastic straw.

Electrical Resistivity Measurements. Resistivity measurements along the 1D chain direction were performed on several single crystals by the two-probe method using the Quantum Design PPMS instrument because the microcracks that develop during a first-order phase transition make it difficult to measure by the four-probe method. We confirmed that the difference in the resistance values in the RT phase measured by the two- and four-probe methods is negligible. The current was measured under a constant applied voltage using the Keithley 6517 electrometer. Electrical contacts between the sample and 15 μm o.d. gold wires were created using silver paint.

DFT Calculations. To perform DFT calculations, we constructed model structures comprising single (monomer), double (dimer), and triple (trimer) Rh(3,6-DBSQ-4,5-(MeO)$_2$)(CO)$_2$ units, as illustrated in Figure S13. The atomic coordinates of the model structures were taken from X-ray crystallographic data. All calculations were performed using an unrestricted B3LYP (UB3LYP) method with basis sets of MIDI + polarization function, 6-31G*, and 6-31+G* for the Rh atoms, 3,6-DBSQ-4,5-(MeO)$_2$ ligand, and CO ligands, respectively. All calculations are carried out using the Gaussian 09 program.[61]

■ ASSOCIATED CONTENT

ⓢ Supporting Information

Additional X-ray crystallographic data, DSC, magnetic data, DFT calculations, UV−vis−near-IR and mid-IR spectral data, electrical resistivity measured with and without an applied magnetic field, and complete ref 61. This material is available free of charge via the Internet at http://pubs.acs.org.

■ AUTHOR INFORMATION

Corresponding Authors
mitsumi@sci.u-hyogo.ac.jp
kitagawa@chem.sci.osaka-u.ac.jp
miyazaki@chem.sci.osaka-u.ac.jp

Present Address
¶Department of Chemical Physics, Faculty of Chemistry, Jagiellonian University, Ingardena 3, 30-060 Kraków, Poland

Notes
The authors declare no competing financial interest.

■ ACKNOWLEDGMENTS

■ REFERENCES

(1) Coronado, E.; Galán-Mascarós, J. R.; Gómez-García, C. J.; Laukhin, V. *Nature* **2000**, *408*, 447−449.

(2) Cui, H.; Wang, Z.; Takahashi, K.; Okano, Y.; Kobayashi, H.; Kobayashi, A. *J. Am. Chem. Soc.* **2006**, *128*, 15074−15075.

(3) Nuida, T.; Matsuda, T.; Tokoro, H.; Sakurai, S.; Hashimoto, K.; Ohkoshi, S.-i. *J. Am. Chem. Soc.* **2005**, *127*, 11604−11605.

(4) Sato, O.; Iyoda, T.; Fujishima, A.; Hashimoto, K. *Science* **1996**, *272*, 704−705.

(5) Coronado, E.; Martí-Gastaldo, C.; Navarro-Moratalla, E.; Burzurí, E.; Camón, A.; Luis, F. *Adv. Mater.* **2011**, *23*, 5021−5026.

(6) Zhou, B.; Idobata, Y.; Kobayashi, A.; Cui, H.; Kato, R.; Takagi, R.; Miyagawa, K.; Kanoda, K.; Kobayashi, H. *J. Am. Chem. Soc.* **2012**, *134*, 12724−12731.

(7) Robertson, C. M.; Leitch, A. A.; Cvrkalj, K.; Myles, D. J. T.; Reed, R. W.; Dube, P. A.; Oakley, R. T. *J. Am. Chem. Soc.* **2008**, *130*, 14791−14801.

(8) Kahn, O.; Martinez, C. J. *Science* **1998**, *279*, 44−48.

(9) Llusar, R.; Uriel, S.; Vicent, C.; Clemente-Juan, J. M.; Coronado, E.; Gómez-García, C. J.; Braïda, B.; Canadell, E. *J. Am. Chem. Soc.* **2004**, *126*, 12076−12083.

(10) Kahn, O.; Launay, J. P. *Chemtronics* **1988**, *3*, 140−151.

(11) Fujita, W.; Awaga, K. *Science* **1999**, *286*, 261−262.

(12) Brusso, J. L.; Clements, O. P.; Haddon, R. C.; Itkis, M. E.; Leitch, A. A.; Oakley, R. T.; Reed, R. W.; Richardson, J. F. *J. Am. Chem. Soc.* **2004**, *126*, 8256−8265.

(13) Clarke, C. S.; Jornet-Somoza, J.; Mota, F.; Novoa, J. J.; Deumal, M. *J. Am. Chem. Soc.* **2010**, *132*, 17817−17830.

(14) D'Avino, G.; Grisanti, L.; Guasch, J.; Ratera, I.; Veciana, J.; Painelli, A. *J. Am. Chem. Soc.* **2008**, *130*, 12064−12072.

(15) Jeannin, O.; Clérac, R.; Fourmigué, M. *J. Am. Chem. Soc.* **2006**, *128*, 14649−14656.

(16) Schmidt, R. D.; Shultz, D. A.; Martin, J. D.; Boyle, P. D. *J. Am. Chem. Soc.* **2010**, *132*, 6261−6273.

(17) Tao, J.; Maruyama, H.; Sato, O. *J. Am. Chem. Soc.* **2006**, *128*, 1790−1791.

(18) Coronado, E.; Galán-Mascarós, J. R.; Monrabal-Capilla, M.; García-Martínez, J.; Pardo-Ibáñez, P. *Adv. Mater.* **2007**, *19*, 1359−1361.

(19) Varret, F.; Bleuzen, A.; Boukheddaden, K.; Bousseksou, A.; Codjovi, E.; Enachescu, C.; Goujon, A.; Linares, J.; Menendez, N.; Verdaguer, M. *Pure Appl. Chem.* **2002**, *74*, 2159−2168.

(20) Lim, S. J.; An, B. K.; Jung, S. D.; Chung, M. A.; Park, S. Y. *Angew. Chem., Int. Ed.* **2004**, *43*, 6346−6350.

(21) Matsuzaki, H.; Fujita, W.; Awaga, K.; Okamoto, H. *Phys. Rev. Lett.* **2003**, *91*, 017403−017401−017404.

(22) Ohtani, R.; Yoneda, K.; Furukawa, S.; Horike, N.; Kitagawa, S.; Gaspar, A. B.; Muñoz, M. C.; Real, J. A.; Ohba, M. *J. Am. Chem. Soc.* **2011**, *133*, 8600−8605.

(23) Nihei, M.; Sekine, Y.; Suganami, N.; Nakazawa, K.; Nakao, A.; Nakao, H.; Murakami, Y.; Oshio, H. *J. Am. Chem. Soc.* **2011**, *133*, 3592−3600.

(24) Sato, O.; Tao, J.; Zhang, Y.-Z. *Angew. Chem., Int. Ed.* **2007**, *46*, 2152−2187.

(25) Clemente-León, M.; Coronado, E.; López-Jordà, M.; Waerenborgh, J. C.; Desplanches, C.; Wang, H.; Létard, J.-F.; Hauser, A.; Tissot, A. *J. Am. Chem. Soc.* **2013**, *135*, 8655−8667.

(26) Coronado, E.; Giménez-Marqués, M.; Martí-Gastaldo, C.; Espallargas, G. M.; Navarro-Moratalla, E.; Waerenborgh, J. C. *Inorg. Chem.* **2013**, *52*, 8451−8460.

(27) Coronado, E.; Espallargas, G. M. *Chem. Soc. Rev.* **2013**, *42*, 1525−1539.

(28) Itkis, M. E.; Chi, X.; Cordes, A. W.; Haddon, R. C. *Science* **2002**, *296*, 1443−1445.

(29) Miller, J. S. *Angew. Chem., Int. Ed.* **2003**, *42*, 27−29.

(30) Leitch, A. A.; Lekin, K.; Winter, S. M.; Downie, L. E.; Tsuruda, H.; Tse, J. S.; Mito, M.; Desgreniers, S.; Dube, P. A.; Zhang, S.; Liu, Q.; Jin, C.; Ohishi, Y.; Oakley, R. T. *J. Am. Chem. Soc.* **2011**, *133*, 6051−6060.

(31) Mailman, A.; Winter, S. M.; Yu, X.; Robertson, C. M.; Yong, W.; Tse, J. S.; Secco, R. A.; Liu, Z.; Dube, P. A.; Howard, J. A. K.; Oakley, R. T. *J. Am. Chem. Soc.* **2012**, *134*, 9886−9889.

(32) Hoshino, N.; Iijima, F.; Newton, G. N.; Yoshida, N.; Shiga, T.; Nojiri, H.; Nakao, A.; Kumai, R.; Murakami, Y.; Oshio, H. *Nat. Chem.* **2012**, *4*, 921−926.

(33) Miyasaka, H.; Motokawa, N.; Chiyo, T.; Takemura, M.; Yamashita, M.; Sagayama, H.; Arima, T. H. *J. Am. Chem. Soc.* **2011**, *133*, 5338−5345.

(34) Isono, T.; Kamo, H.; Ueda, A.; Takahashi, K.; Nakao, A.; Kumai, R.; Nakao, H.; Kobayashi, K.; Murakami, Y.; Mori, H. *Nat. Commun.* **2013**, *4*, 1344.

(35) Lange, C. W.; Földeàki, M.; Nevodchikov, V. I.; Cherkasov, V. K.; Abakumov, G. A.; Pierpont, C. G. *J. Am. Chem. Soc.* **1992**, *114*, 4220−4222.

(36) Nevodchikov, V. I.; Abakumov, G. A.; Cherkasov, V. K.; Razuvaev, G. A. *J. Organomet. Chem.* **1981**, *214*, 119−124.

(37) Pierpont, C. G. *Coord. Chem. Rev.* **2001**, *216−217*, 99−125.

(38) Dei, A.; Gatteschi, D.; Sangregorio, C.; Sorace, L. *Acc. Chem. Res.* **2004**, *37*, 827−835.

(39) Sato, O.; Cui, A.; Matsuda, R.; Tao, J.; Hayami, S. *Acc. Chem. Res.* **2007**, *40*, 361−369.

(40) Mitsumi, M.; Goto, H.; Umebayashi, S.; Ozawa, Y.; Kobayashi, M.; Yokoyama, T.; Tanaka, H.; Kuroda, S.-i.; Toriumi, K. *Angew. Chem., Int. Ed.* **2005**, *44*, 4164−4168.

(41) Abakumov, G. A.; Nevodchikov, V. I.; Cherkasov, V. K. *Bull. Acad. Sci. USSR, Div.Chem. Sci.* **1985**, *34*, 2507−2514.

(42) Kume, Y.; Miyazaki, Y.; Matsuo, T.; Suga, H. *J. Phys. Chem. Solids* **1992**, *53*, 1297−1304.

(43) Sorai, M.; Nakazawa, Y.; Nakano, M.; Miyazaki, Y. *Chem. Rev.* **2013**, *113*, PR41−PR122.

(44) Adams, D. M.; Dei, A.; Rheingold, A. L.; Hendrickson, D. N. *Angew. Chem., Int. Ed.* **1993**, *32*, 880−882.

(45) Hamilton, W. C.; Ibers, J. A. *Hydrogen bonding in solids*; W. A. Benjamin, Inc.: New York, 1968.

(46) Gilli, G.; Gilli, P. *The nature of the hydrogen bond, outline of a comprehensive hydrogen bond theory*; Oxford University Press: Oxford, 2009.

(47) Estes, W. E.; Gavel, D. P.; Hatfield, W. E.; Hodgson, D. J. *Inorg. Chem.* **1978**, *17*, 1415−1421.

(48) Hall, J. W.; Marsh, W. E.; Weller, R. R.; Hatfield, W. E. *Inorg. Chem.* **1981**, *20*, 1033−1037.

(49) Borrás-Almenar, J. J.; Coronado, E.; Curely, J.; Georges, R.; Gianduzzo, J. C. *Inorg. Chem.* **1994**, *33*, 5171−5175.

(50) Baker, G. A., Jr.; Rushbrooke, G. S.; Gilbert, H. E. *Phys. Rev.* **1964**, *135*, A1272−A1277.

(51) Fisher, M. E. *Am. J. Phys.* **1964**, *32*, 343−346.

(52) O'Connor, C. J. *Prog. Inorg. Chem.* **1982**, *29*, 203−283.

(53) Carlin, R. L. *Magnetochemistry*; Springer-Verlag: Berlin, 1986.

(54) Kahn, O. *Molecular magnetism*; VCH Publishers: New York, 1993.

(55) Weng, D.-F.; Wang, Z.-M.; Gao, S. *Chem. Soc. Rev.* **2011**, *40*, 3157−3181.

(56) Dzyaloshinsky, I. *J. Phys. Chem. Solids* **1958**, *4*, 241−255.

(57) Moriya, T. *Phys. Rev.* **1960**, *120*, 91−98.

(58) Coulon, C.; Miyasaka, H.; Clérac, R. *Struct. Bonding (Berlin)* **2006**, *122*, 163−206.

(59) Zhang, W.-X.; Ishikawa, R.; Breedlove, B.; Yamashita, M. *RSC Adv.* **2013**, *3*, 3772−3798.

(60) Numata, Y.; Inoue, K.; Baranov, N.; Kurmoo, M.; Kikuchi, K. *J. Am. Chem. Soc.* **2007**, *129*, 9902−9909.

(61) Frisch, M. J. et al. *Gaussian 09*, revision C.01; Gaussian, Inc.: Wallingford, CT, 2009.

(62) Soda, T.; Kitagawa, Y.; Onishi, T.; Takano, Y.; Shigeta, Y.; Nagao, H.; Yoshioka, Y.; Yamaguchi, K. *Chem. Phys. Lett.* **2000**, *319*, 223−230.

(63) Shoji, M.; Koizumi, K.; Kitagawa, Y.; Kawakami, T.; Yamanaka, S.; Okumura, M.; Yamaguchi, K. *Chem. Phys. Lett.* **2006**, *432*, 343−347.

(64) Yamaguchi, K. *Int. J. Quantum Chem.* **1980**, *18*, 101−106.

(65) Kobayashi, A.; Sasa, M.; Suzuki, W.; Fujiwara, E.; Tanaka, H.; Tokumoto, M.; Okano, Y.; Fujiwara, H.; Kobayashi, H. *J. Am. Chem. Soc.* **2004**, *126*, 426−427.

(66) Hanasaki, N.; Tajima, H.; Matsuda, M.; Naito, T.; Inabe, T. *Phys. Rev. B* **2000**, *62*, 5839−5842.

(67) Matsushita, M.; Kawakami, H.; Sugawara, T.; Ogata, M. *Phys. Rev. B* **2008**, *77*, 195208−195201−195206.

(68) Mitsumi, M.; Murase, T.; Kishida, H.; Yoshinari, T.; Ozawa, Y.; Toriumi, K.; Sonoyama, T.; Kitagawa, H.; Mitani, T. *J. Am. Chem. Soc.* **2001**, *123*, 11179−11192.

(69) Perrin, D. D.; Armarego, W. L. F. *Purification of laboratory chemicals*; Pergamon Press: New York, 1988.

(70) Martinengo, S.; Gxordano, G.; Chini, P.; Parshall, G. W.; Wonchoba, E. R. *Inorg. Synth.* **1990**, *28*, 242−245.

(71) Vol'eva, V. B.; Novikova, I. A.; Ivanova, E. V.; Ershov, V. V. *Russ. Chem. Bull.* **1986**, *35*, 199−202.

(72) Mitsumi, M.; Umebayashi, S.; Ozawa, Y.; Tadokoro, M.; Kawamura, H.; Toriumi, K. *Chem. Lett.* **2004**, *33*, 970−971.

(73) *CrystalClear*, version 1.3; Rigaku Corporation: Tokyo, Japan, 2000.

(74) Altomare, A.; Burla, M. C.; Camalli, M.; Cascarano, G. L.; Giacovazzo, C.; Guagliardi, A.; Moliterni, A. G. G.; Polidori, G.; Spagna, R. *J. Appl. Crystallogr.* **1999**, *32*, 115−119.

(75) Sheldrick, G. M. *SHELXL-97, Program for crystal structure determination*; University of Göttingen: Göttingen, Germany, 1997.

(76) Wakita, K. *Yadokari-XG, Software for crystal structure analyses*, 2001.

(77) Kabuto, C.; Akine, S.; Nemoto, T.; Kwon, E. *J. Cryst. Soc. Jpn.* **2009**, *51*, 218−224.